

Wave measurements from ship mounted sensors in the Arctic marginal ice zone

Trygve. K. Løken^{a,1}, Jean Rabault^a, Atle Jensen^a, Graig Sutherland^b, Kai H. Christensen^c
and Malte Müller^c

^a Department of Mathematics, University of Oslo, Oslo, Norway

^b Environment and Climate Change Canada, Québec, Canada

^c Norwegian Meteorological Institute, Oslo, Norway

Abstract

Increased research interest and economic activity in the Arctic raise the need for new observations of sea ice dynamics. Remote sensing as well as mathematical and numerical models of wave propagation in sea ice would benefit from more in situ data for validation. This study presents wave measurements in the marginal ice zone (MIZ) obtained from ship mounted sensors. The system combines altimeter readings from the ship bow with ship motion correction data to provide estimated single point ocean surface elevation. Significant wave height and mean wave period, as well as one-dimensional wave spectra are derived from the combined measurements. The results are compared with integrated parameters from a spectral wave model over a period of eight days in the open ocean, and with spectra and integrated parameters derived from motion detecting instruments placed on ice floes inside the MIZ. Mean absolute errors of the integrated parameters are in the range 15.0-18.9% when comparing with the spectral wave model and 1.0-9.6% when comparing with valid motion detecting instruments. The spatial wave damping coefficient is estimated by looking at the change in spectral wave amplitude found at discrete frequency values as the ship was moving along the longitudinal direction of the MIZ within time intervals where the wave field is found to be approximately constant in time. As expected from theory, high frequency waves are effectively dampened by the presence of sea ice. The observed wave attenuation rates compare favourably with a two-layer dissipation model. Our methodology can be regarded as a simple and reliable way to collect more waves-in-ice data as it can be easily added to any ship participating to ice expeditions, at little extra cost.

Keywords: Sea ice dynamics, wave measurements, marginal ice zone, wave attenuation

1 Introduction

Sea ice is a major feature in the polar environments, it has importance for Arctic ecosystems as well as for global ocean and atmospheric circulation. A decline in the Arctic ice cover has been observed over the past decades (Feltham, 2015). Interactions between sea ice and surface gravity waves play an important role in breakup and reduction of ice cover. The decline in ice cover leads to a larger fetch where waves build up more energy and enhance the breakup and melting process in a feedback mechanism (Thomson & Rogers, 2014). The mixture of icebergs, floes and grease ice found in the interface between solid ice, such as land fast ice or pack ice, and the open ocean, is called the marginal ice zone (MIZ). Previous studies have found that high frequency wind waves are effectively dampened in the MIZ (Weber, 1987; Wadhams *et al.*, 1988), which reduces the ice cover break up rate.

Recent changing conditions in the polar regions have allowed for increased human activities, which raises the importance of better forecast models and improved physical understanding of the environment to ensure safe operations (Fritzner *et al.*, 2019). In situ wave measurements can increase our

¹E-mail address and phone number for corresponding: trygvekl@math.uio.no (+47) 94885767 (T.K. Løken)

E-mail addresses: jeanra@math.uio.no (J. Rabault), atlej@math.uio.no (A. Jensen),

graugory.sutherland@canada.ca (G. Sutherland), kaihc@met.no (K.H. Christensen), maltem@met.no (M. Müller).

understanding of global climate systems and provide data for calibration of numerical models. Also, mathematical models to describe wave attenuation in ice, e.g. Weber (1987), Newyear & Martin (1997) and (Sutherland *et al.*, 2019), need experimental data for validation and improvement. However, experimental data are relatively sparse due to the inaccessibility of the regions where sea ice is present, combined with the harsh and dangerous environment for both researchers and instruments (Squire, 2007).

We present here results from shipborne wave measurements in the MIZ. This system has not up until now been used deep into the MIZ, therefore, the novelty of our observations. The methodology, first described in Christensen *et al.* (2013), combines a bow mounted altimeter and a motion correction device. We provide wave spectra and integrated parameters from spectra, which are important quantities when considering wave-ice interactions. Significant wave height and mean periods are compared with a spectral wave forecast model over a period of eight days in the open ocean. We also compare measurements in the MIZ with data from wave measuring instruments consisting of inertial motion units (IMUs) placed on ice floes (Rabault *et al.*, 2019). From the spectra, the spatial damping coefficient is found as a function of wave frequency, which can be compared to attenuation models.

In this paper, the data acquisition and processing methods are described in Section 2. The results are presented in Section 3, which is divided in two parts. A comparison with spectral model and in situ instruments is outlined in Section 3.1. In Section 3.2, we present results on wave attenuation and the spatial damping coefficient is compared to the theoretical model of (Sutherland *et al.*, 2019). Finally, a discussion follows in Section 4 and the concluding remarks are given in Section 5.

2 Data and Methods

The data were obtained during a research campaign in the Barents Sea with R/V Kronprins Haakon in September 2018 as part of the Nansen Legacy project (Reigstad *et al.*, 2017). The vessel is 100 m long and with a beam of 21 m. In total, the cruise lasted two weeks, during which continuous measurements were made. The results from the MIZ presented here were recorded on September 19 when the ship ventured approximately 28 km into the MIZ. Four stops were made to deploy in situ waves-in-ice (WII) instruments on ice floes (Rabault *et al.*, 2019), which were used to validate our ship mounted system. Upon the return to the open ocean, a total of seven stops were made with more or less equal spacing on a close to straight south-southwest heading where measurements for wave damping estimates were carried out. Twenty minutes samples were recorded as the ship was freely drifting on each station. The location, starting time and wave travel distance (WTD) for each measurement in the MIZ are summarized in Table 1. Prefix 1 denotes the four stops into the MIZ while prefix 2 denotes the seven stops out of the MIZ.

Stop	Time	Position (N/E)	WTD [km]
1.1	04:22	82.126/20.736	
1.2	06:28	82.246/20.245	
1.3	08:59	82.355/19.803	
1.4	12:20	82.436/19.674	
2.1	13:11	82.421/19.579	92.7
2.2	14:32	82.359/19.544	69.2
2.3	15:40	82.294/19.389	58.3
2.4	16:54	82.228/19.275	20.8
2.5	18:00	82.163/19.183	6.7
2.6	19:08	82.099/19.046	0
2.7	20:09	81.994/18.982	0

Table 1: Time and location where measurements were carried out inside the MIZ. Prefix 1 for stop number indicate deployment of WII instruments while prefix 2 indicate measurement of damping coefficient. WTD through the MIZ are listed for the stops with prefix 2.

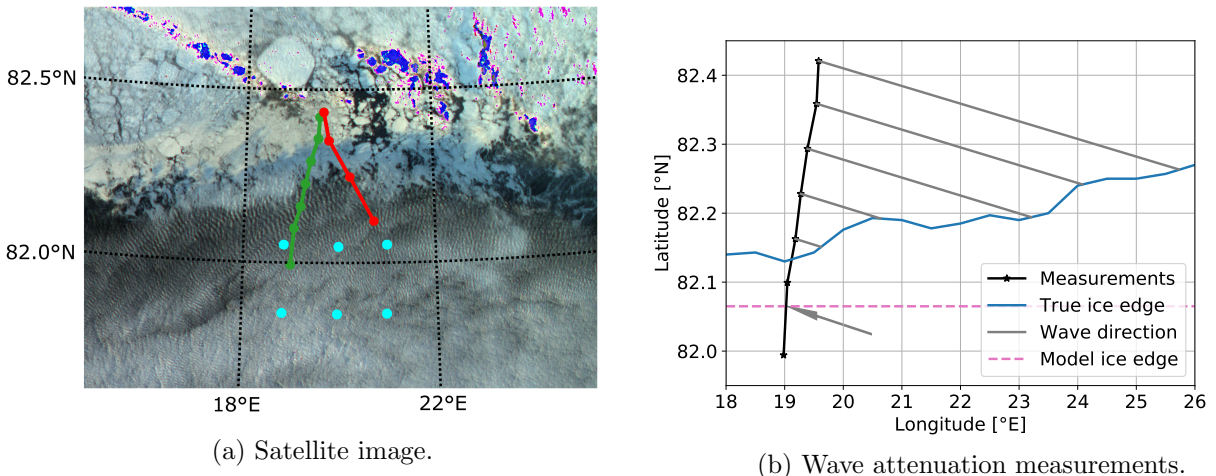


Figure 1: MIZ and location of measurements. a) Satellite image with ship trajectory into (red) and out of (green) the MIZ. Cyan dots mark the location where wave parameters from the spectral model are extracted to check for constant sea state. b) Wave direction from spectral model and WTD through the ice for each measurement (used for wave damping coefficient). The ice edge found from satellite image and the one used in the spectral model are indicated.

Figure 1a shows the ship trajectory into (red) and out of (green) the MIZ and the ice edge at approximately 82.2 °N below the thin cloud cover. The ice concentration for the four stops 1.1-1.4 was estimated to be roughly 10%, 30%, 90% and 100% respectively in Rabault *et al.* (2019). The ice edge is roughly recreated from the satellite image and shown in Fig. 1b along with the location of the wave attenuation measurements, i.e. stops 2.1-2.7. This figure also indicates the ice edge used in the spectral model and the mean wave direction on September 19 estimated by the spectral model, which is further described in Section 2.5. We use the "going-to" convention for wave direction and ship heading and the "coming-from" convention for wind direction and define directions as clockwise rotation from the geographic north. The gray lines illustrate the WTD through the ice for each stop.

2.1 Data acquisition

The instrument setup consisted of an ultrasonic gauge (UG) that measured ocean surface elevation relative to the ship bow. Figure 2a and 2b shows the downward facing UG mounted on a rigid pole.

Estimated absolute surface elevation was obtained after correcting for ship motion by means of an IMU placed on deck, also in the bow section of the ship. The horizontal and vertical distances between the UG and the IMU were $x_{lev} = 2.5$ m and $y_{lev} = 6$ m respectively.



(a) UG seen from the front.



(b) UG seen from above.

Figure 2: Installation of the downward facing UG on a rigid pole in the ship bow.

We used a UG (Banner QT50ULB) with approximately 0.2-8 m range. The instrument emits 75 kHz ultrasonic pulses at a 10.4 Hz sampling rate. Distance L between the UG and the ocean surface is calculated internally from the time delay of the echo, where the speed of sound in air is temperature compensated with an integrated thermometer. Mean L was approximately 5 m and the effective beam width, i.e. the diameter of the circular area where the signal was reflected on the ocean surface, was approximately 0.9 m. This footprint is very low compared to the wavelength $\lambda = 156$ m of a typical 0.1 Hz ocean wave, as the one shown in Fig. 4. The wavelength is found from $\lambda = 2\pi/k$, and the wavenumber k from the linear deep water dispersion relation:

$$\omega^2 = gk, \quad (1)$$

where $\omega = 2\pi f$ is the angular frequency, f the wave frequency and g the acceleration due to gravity. The depth dependency is neglected here since the water depth was ≈ 3500 m in the region. The use of (1) in the MIZ can be justified by the fact that the dispersion relation in ice deviates little from the deep water dispersion relation in the frequency band where wave motion is present (Marchenko *et al.*, 2017).

A feature of the UG called Auto-Window was enabled, meaning that a 1 m sensing window was centered around a taught length. The taught length \bar{L} was found automatically by time averaging L over a couple of wave periods before each measurement was initiated. We later display the output signal of the instrument as $D = L - \bar{L}$ in Figures 4, 5a and 5b. The Auto-Window feature was chosen out of practical reasons at the expense of a reduced range ($|D| < 0.5$ m), because the intention was initially to only measure in the MIZ where lower trough-to-crest amplitudes than 1 m are normally expected. However, it was decided to measure continuously during the whole cruise, also in the open ocean where the waves were generally larger than in the MIZ. Consequently, the instrument range was exceeded (saturated) at times with large wave amplitudes. We define a low saturation when $D < -0.5$ m and a high saturation when $D > +0.5$ m. In these cases, the output signal of D is simply ± 0.5 m, although the distance is actually smaller or greater, and this can be seen as a "cut" graph in Fig. 5b. We define the saturation proportion as the ratio of time where saturation occurs over total sample time. Figure 3 shows the saturation proportion of each sample for stops 2.1-2.7, where "total" saturation proportion is the sum of "low" and "high" saturation proportion. We accept up to 10% total saturation and will therefore discard the sample recorded at stop 2.7, which had a total saturation of approximately 20%, in our wave attenuation analysis in Section 3.2.

The system can measure trough-to-crest amplitudes up to 1 m before the range of the UG is exceeded. This constraint sets an upper limit for how large significant wave height the instrument

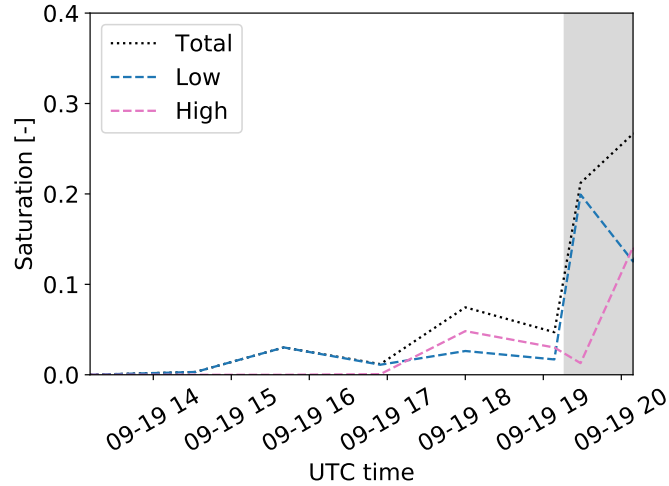


Figure 3: Saturation proportion (i.e. proportion of time when the UG range was exceeded) for stops 2.1-2.7, where "total" saturation proportion is the sum of "low" and "high" saturation proportion. Area of discarded data due to total saturation exceeding 10% threshold is shaded.

theoretically can record in a time series without exceeding the measurement range. Significant wave height (SWH) from time series is defined as:

$$SWH = 4\sigma, \quad (2)$$

where σ is the standard deviation of the surface elevation η . In the simplified case of a pure sine wave, the trough-to-crest amplitude is equal to $2\sqrt{2}\sigma$. In this idealized example where ship motion is not considered, the limiting upper value of SWH is approximately 1.4 m for the UG.

As motion correction device, we used an IMU (VectorNav VN100) similar to the ones in Rabault *et al.* (2019). It features 3-axis accelerometers and 3-axis gyroscopes measuring at a rate of 800 Hz. After an internal Kalman filtering, the instrument gives an output frequency of 80 Hz. The gyros yield rotation angles about all three axis directly. Vertical acceleration is integrated twice to obtain ship vertical displacement about the mean, where positive values are displacement above the mean. Details on the integral scheme, data filtering and other technical information on the instrument can be found in Rabault *et al.* (2019).

In order to obtain time series of the surface elevation, UG and IMU data at the same time instance were needed. We solved this by defining a common sampling rate of 10 Hz, which should be sufficient for resolving all relevant ocean surface features. All data were then interpolated on the common time base for the analysis.

2.2 Ship response

In general, if the wavelength λ is large when compared with the diameter d of a floating body, the body will tend to follow the path of a fluid particle at the free surface. In the opposite case when λ/d is small, the waves are losing their influence on the behavior of the body. The response amplitude operator (RAO) of a vessel (or any object) is the ratio of response amplitude over incoming wave amplitude. RAOs in all modes for R/V Kronprins Haakon are reported in Ytterland (2016). RAOs depend on the wave heading angle β , which is defined as the relative angle between the ship heading and wave direction. Hence, $\beta = 0^\circ$ corresponds to following seas, $\beta = 90^\circ$ corresponds to beam seas, and $\beta = 180^\circ$ corresponds to head seas.

2.3 Motion correction

Downwards facing altimeters mounted on fixed structures are common for measuring ocean surface elevation η , which is a function of time (Reistad *et al.*, 2011; Magnusson & Donelan, 2013). Correction

is required when the altimeter is mounted on a floating structure like a ship. The parameter η is a function of the position in the horizontal plane in addition to time when the ship is free to move, but we assume the horizontal drift velocity to be much smaller than the phase speed of the waves, so that the dependency of position can be neglected. We define a coordinate system with the (x, y, z) axis to be aligned horizontally in the direction from stern to bow, vertically in upward direction and horizontally in the direction from port to starboard, respectively. The origin coincides with the IMU. Along axis translation are surge, heave and sway while rotation about the axis are roll, yaw and pitch, respectively. Only the vertical modes, heave ξ , roll angle ϕ_R and pitch angle ϕ_P affect the distance L measured by the UG and need to be addressed when compensating.

In the (imaginary) case where the ship lies completely still, as if it was fixed in position, surface elevation will be given by $\eta = \bar{L} - L$. When heave response is present, we simply subtract the vertical displacement ξ , which is positive when the ship is above its mean level and negative when the ship is below. When rotation about the horizontal axis is included, two aspects need to be considered. First, the UG measures the distance to the surface with an angle about the vertical axis. The true vertical distance is obtained by multiplying L with the cosine of both ϕ_R and ϕ_P as shown in the second term on the R.H.S. of (3). Second, there is the lever effect due to the horizontal and vertical distance between the UG and the IMU, x_{lev} and y_{lev} respectively. The UG is displaced in vertical direction relative to the ocean surface when the UG rotates around the IMU about the x -axis and the y -axis, which corresponds to ship roll and pitch respectively. We name these displacements roll and pitch elevation effects, and define them respectively as $y_{lev}(1 - \cos(\phi_R))$, which is always positive, and $x_{lev}\sin(\phi_P)$, which is positive when the bow is above the rotational center of the ship and negative otherwise.

All corrections are combined and we obtain an expression for the ocean surface elevation:

$$\eta = \bar{L} - L\cos(\phi_R)\cos(\phi_P) - \xi - y_{lev}(1 - \cos(\phi_R)) - x_{lev}\sin(\phi_P), \quad (3)$$

which is similar to Eq. 1 in Christensen *et al.* (2013) except from the roll and pitch elevation effects in the fourth and fifth term on the R.H.S. of (3), which are new considerations.

A typical example of a 150 s time series inside the MIZ is shown in Fig. 4. Trough-to-crest amplitudes up to approximately 0.4 m and frequencies of around 0.1 Hz are found in this specific sample, as seen in the upper panel. Ship heave response ξ and UG reading $D = L - \bar{L}$ are also presented in the upper panel and are in the same order of magnitude as the surface elevation. The lower panel shows roll and pitch elevation effects (fourth and fifth term on R.H.S. of (3) respectively) in addition to the UG angle correction factor corresponding to the second term on R.H.S. of (3), here presented as $1 - \cos(\phi_R)\cos(\phi_P)$. These results indicate that the roll elevation effect and the UG angle correction factor are $\mathcal{O}(10^{-3})$ relative to the wave amplitude and thus negligible in this case. The pitch elevation effect is on the other hand approximately 0.02 m and $\mathcal{O}(10^{-1})$ relative to the wave amplitude and is therefore important to include in the processing.

A section of the time series from stop number 1.1 is presented in Fig. 5a, where the mean value of the surface elevation η jumps from zero up to about 0.1 m after roughly 35 s and then jumps back to zero at roughly 100 s. This step is most likely caused by an ice floe drifting under the sensing window of the UG for a short period and demonstrates the UG's ability to receive reflected signals off an ice cover. The crest-to-trough amplitude is approximately 0.4 m for the waves and 0.1 m for the step. If the step is interpreted as a long wave, its frequency is less than 0.015 Hz, which is much lower than the lower cut-off frequency f_{min} in the spectral analysis, explained in Section 2.4.

An example of a saturated sample can be seen in Fig. 5b. This time series is extracted from stop number 2.7. The UG reading D , is clearly flattened out at the peaks where the range of the instrument is exceeded. Total saturation for this sample was approximately 20%.

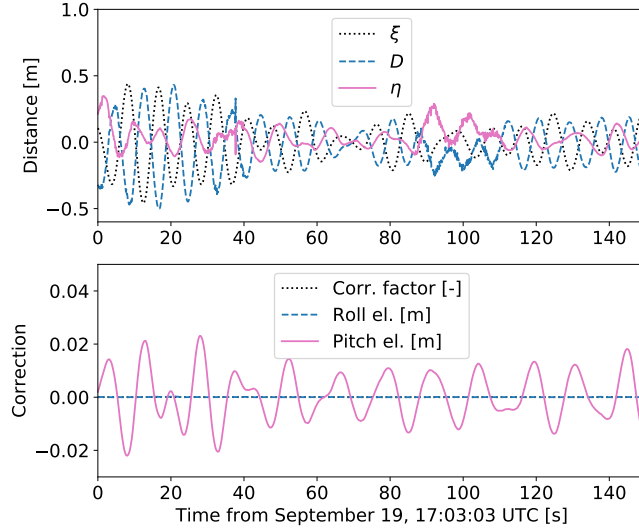


Figure 4: 150 s time series of UG and IMU measurements from stop 2.4. In upper panel: Ship heave response ξ , UG-reading D and surface elevation η . In lower panel: UG angle correction factor (corresponds to the second term on R.H.S. of (3), displayed with black dotted line), roll and pitch elevation effect (fourth and fifth term on R.H.S. of (3) respectively).

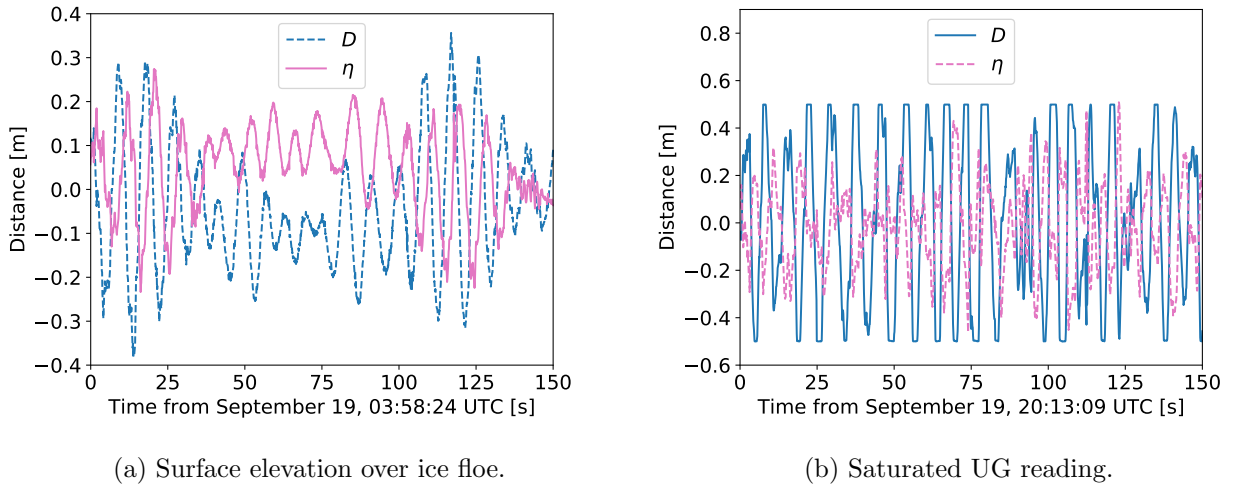


Figure 5: Time series of UG-reading D and surface elevation η . a) Stop 1.1 where an ice floe most likely drifts under the sensing window of the instrument. b) Stop 2.7 with approximately 20% saturated UG signal.

2.4 Statistical parameters and spectrum

We obtain surface elevation from (3). Power spectrum density $PSD(f)$ of the surface elevation is obtained with the Welch method (Earle, 1996) where the samples are subdivided in q consecutive segments and ensemble averaged. Segment size is set to 200s with 50 % overlap. With 20 min sampling time at 10 Hz common sampling rate, this gives a segment size of 2000 sampling points and a total number of 12000 sampling points for each measurement. A Hanning window is applied to each segment to reduce spectral leakage.

Since we are later comparing our measurements with data from a spectral model, we find the statistical parameters from spectra. The mean wave period and the significant wave height are obtained

from the spectral moments:

$$m_j = \int_{f_{min}}^{f_{max}} f^j PSD(f) df, \quad (4)$$

where the cutoff frequencies f_{min} and f_{max} are set to 0.04 Hz and 1.0 Hz respectively, which should include the most energetic ocean waves. The same cutoff frequencies are applied in the spectral model we have compared our results with. In our comparison of integrated parameters from bow instruments and WII instruments at stops 1.1-1.4, we use 0.05-0.25 Hz, which corresponds to the cutoff frequencies applied by the on-board processing unit of the WII instruments. The spectral moments can be used to estimate the mean (T_{m01}) and zero up-crossing (T_{m02}) periods from

$$T_{m01} = \frac{m_0}{m_1}, \quad (5)$$

and

$$T_{m02} = \sqrt{\frac{m_0}{m_2}}, \quad (6)$$

respectively.

We use significant wave height H_s from spectra for most of our analysis here. SWH from time series of surface elevation (Eq. 2) is used for comparison in a redundancy check for the measurements, as the two methods ideally should yield the same result. H_S is defined as:

$$H_s = 4\sqrt{m_0}. \quad (7)$$

Wave attenuation is dependent on frequency. It is therefore convenient to have a measure for wave amplitude as function of frequency when finding the spatial damping coefficient. We define a spectral amplitude a at discrete forcing frequency f_0 as:

$$a(f_0) = \sqrt{\int_{f_0-\Delta f}^{f_0+\Delta f} PSD(f) df}, \quad (8)$$

where Δf is the bandwidth frequency set to 0.005 Hz. Six discrete forcing frequencies (0.076-0.128 Hz with 0.0104 Hz increments) are chosen based on the spectra presented in Section 3.2. Equation 8 is similar to the definition of Meylan *et al.* (2014), used for attenuation analysis in the Antarctic MIZ. The spectral amplitude $a(f_0)$ is not the physical wave amplitude in the classical sense, but an interpretation of the energy content in a finite frequency proportion of the PSD with unit meter.

Confidence intervals for both spectra and the integrated parameters, significant wave height and amplitude, are calculated from the Chi-squared distribution, following the methodology presented in Young (1995). For spectra, the total degree of freedom (TDF) is calculated as $TDF = 2q$, and for significant wave height, TDF is found with Eq. 9 below (ITTC, 2017).

$$TDF = \frac{2q \left[\int_{f_{min}}^{f_{max}} PSD(f) df \right]^2}{\int_{f_{min}}^{f_{max}} [PSD(f)]^2 df}. \quad (9)$$

Equation 9 is also used when finding the confidence intervals for $a(f_0)$, with the small modification of multiplying the bandwidth frequency Δf to the denominator.

We use the mean absolute percentage error (MAPE) to compare our system with either the spectral model or the WII instruments. Systematic bias is described with the mean percentage error (MPE). The error statistics are defined as:

$$MAPE = \frac{100\%}{n} \sum_{t=1}^n \left| \frac{X_t - Y_t}{X_t} \right|, \quad (10)$$

$$MPE = \frac{100\%}{n} \sum_{t=1}^n \frac{X_t - Y_t}{X_t}, \quad (11)$$

where Y_t are parameters obtained from bow measurements and X_t are reference parameters.

2.5 Wave model

We have used the WAM-4 spectral wave forecast model, run operationally by the Norwegian Meteorological Institute (Carrasco & Gusdal, 2014), as a reference to cross-validate our system outside the MIZ. Spatial and temporal resolution of the model is 4 km and 1 hour, respectively, and it runs twice a day. A hard ice boundary based on satellite images (ice concentration over 3/10th) is defined in the model. No wave simulations are performed where the assumed ice cover is present, although the model still provides wind information everywhere within the domain. The model ice edge was defined at 82.065 °N on September 19. From the model, we extract total mean wave direction THQ , H_S , T_{m01} , T_{m02} and wind parameters. The wave parameters are integrated parameters from spectra, but the raw spectra were not available.

2.6 Waves-in-ice instruments

Four in situ WII instruments (Rabault *et al.*, 2019), placed on ice floes close to the ship at the stops 1.1-1.4, have been used to cross-validate our system inside the MIZ. The instruments measure waves with an integrated IMU, and they have been tested and used in a series of previous works (Rabault *et al.*, 2016, 2017; Sutherland & Rabault, 2016; Marchenko *et al.*, 2017). The WII instruments are autonomous and designed to be deployed for long durations. Compressed power spectra from 20 min time series of surface elevation were sent via Iridium satellite and used as comparison with the spectra obtained from the bow measurements. We also compare the integrated parameters H_S and T_{m02} .

The WII instruments measured with five hours intervals to conserve battery power. Data from the first measurement were corrupted due to disturbances during carrying and placement on the ice and were discarded. The results presented here are from the second measurement of each instrument, i.e. five hours after the respective bow measurement. The temporal change of sea state over these five hour periods are addressed in Section 3.1. The WII instruments drifted 2.4 km, 1.7 km, 3.5 km and 2.2 km during the five hours between first sample taken at stop 1.1-1.4 respectively, and second sample. These are relatively small displacements compared to the distance between the WII instruments, which were an order of magnitude larger. Hence, the measurements with the two different systems were made at approximately the same place with five-hour time delay.

2.7 Attenuation modeling

Previous field measurements indicate that waves decay exponentially in ice (Squire & Moore, 1980; Wadhams *et al.*, 1988). For each frequency bin corresponding to the six forcing frequencies f_0 , the spectral amplitudes a are fitted to decreasing exponentials on the shape $a = Ce^{-\alpha x} + c$, where C , α and c are estimated parameters and x is wave traveling distance through the MIZ, by means of non-linear least squares. From the fitted curves, the spatial damping coefficients α , which describe wave attenuation are determined from:

$$\frac{\partial a}{\partial x} = -\alpha a, \quad (12)$$

for each frequency bin. Non-linear least squares are applied to fit a power function $\alpha = Af^p$ to the measured values of α as function of frequency f , where A and p are estimated parameters. The standard error in the exponent is obtained from the square root of the variance of p .

Spatial damping coefficients found in the field measurements are compared to the model of Sutherland *et al.* (2019), which presents a parameterization for wave dissipation that allows for a two-layer structure within the ice. The lower layer with thickness ϵh_i , where h_i is the total ice thickness, is defined as a highly viscous layer where wave motion exists. The upper layer is defined as impermeable. With a no-slip boundary condition imposed on the bottom of the ice, Equation (16) of Sutherland *et al.* (2019) can be written as:

$$\alpha_{mod} = \frac{1}{2}\epsilon h_i k^2, \quad (13)$$

where k is the wavenumber, here calculated with (1). Total ice thickness is set to $h_i = 1.1$ m based on visual observations from the field campaign. We use $\epsilon = 0.02$ due to the large ice thickness, meaning

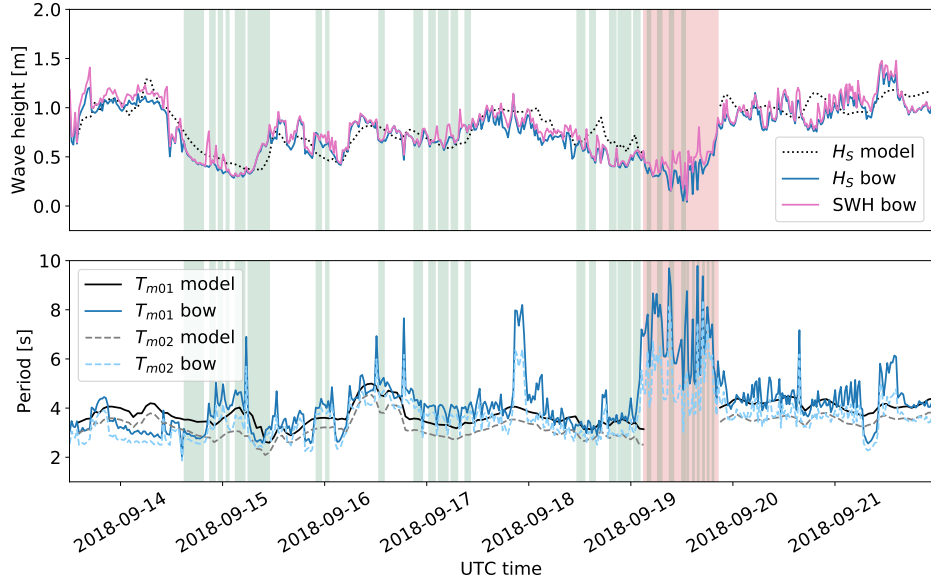


Figure 6: Long time comparison between observations and the WAM-4 model. Significant wave height from time series and spectra (upper), and periods from spectra (lower). Time periods where total saturation is below 10% and ship speed over ground (SOG) is below 0.5 m/s are highlighted with green background color and the period with an ice cover (hence no model data) is highlighted with red background color.

that wave motion is assumed to exist in a small fraction of the total ice thickness. Note that (13) is proportional to the frequency in the fourth power.

3 Results

3.1 Data validation

Bow measurements are compared with spectral model data interpolated to the ship location in Fig. 6. Valid measurements, i.e. time periods where total UG saturation is below 10% and ship speed over ground (SOG) is below 0.5 m/s, are highlighted with green background color. The period with no available model data due to the ice cover is highlighted with red background color. The whole comparison spans over eight days, and periods of valid measurements are found 23% of the time. Error statistics are summarized in Table 2 where MAPE describes the mean absolute error and MPE describes the mean error. In general, there is a good agreement between observations and model, also for the conditions not defined as valid. The MPEs do not exceed $\pm 10\%$ for H_S and T_{m01} in the valid periods, which indicate low systematic bias. A surprising result is that significant wave height has a higher MAPE in the valid periods than outside, although the difference is not large (18.9% vs 13.3%). MAPEs for T_{m01} are about the same inside the valid periods as outside. Note that significant wave height does not exceed the theoretical limit (for sine waves) of 1.4 m as described in Section 2.1 within the valid data periods. MAPE between measured H_S and SWH was 11.7% during valid measurements (not shown in Table 2).

A stationary sea state over the measurement period inside the MIZ is an advantage in our analysis. The sea state is investigated in Fig. 7 where time series of H_S , T_{m01} and THQ from WAM-4 are presented. The model data are extracted from the six points arranged in a grid configuration outside the MIZ, shown in cyan in Fig. 1a. Time series from each grid point are plotted in gray and the mean value in a different color. All parameters were close to constant between 11:00 and 17:00 but varying with time outside of this period. This indicates a variability in sea state in the comparison of bow and WII instruments, due to the five-hour time delay between the measurements. However, the change was not dramatic. From 04:22 to 09:22 at stop 1.1, the standard deviation in the mean samples (containing five values) were 0.06 m, 0.10 s and 1.00° for H_S , T_{m01} and THQ respectively.

	Error	H_S	T_{m01}	T_{m02}
Valid	MAPE [%]	18.9	15.0	17.2
	MPE [%]	9.2	-8.9	-14.4
Not val.	MAPE [%]	13.3	15.7	14.7
	MPE [%]	3.2	-5.5	-4.4

Table 2: Long time error statistics for significant wave height H_S and periods T_{m01} and T_{m02} when comparing bow measurements with the WAM-4 model. Valid periods are defined as when total UG saturation is less than 10% and ship speed over ground is less than 0.5 m/s (23% of the time). All other times are considered not valid.

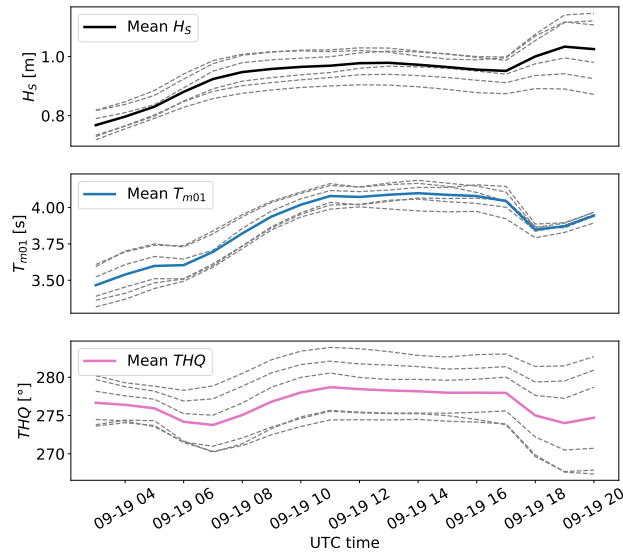


Figure 7: Time series of H_S (upper), T_{m01} (middle) and THQ (lower) from WAM-4 spectral model. Values are extracted from locations indicated by the six cyan colored dots in Fig. 1a and plotted in gray. Mean values are plotted in different colors.

From 12:20 to 17:20 at stop 1.4, the standard deviation in the mean samples are an order lower for all parameters. The results in Fig. 7 also indicate a variability in sea state over the period from 13:11 to 19:08 where wave damping was measured. In this period, the standard deviations in the mean samples (containing seven values) were 0.03 m, 0.10 s and 1.64° for H_S , T_{m01} and THQ respectively.

A comparison of ship measurements and available model data from stops 2.1-2.6 is presented in Fig. 8. The upper panel shows ship heading and speed over ground (SOG), extracted from the ship navigation system. Forecasted wind direction and speed presented in the lower panel are compared to 10 min average values (corrected for ship motion) acquired by the ship anemometer. The six stops when measurements are performed are clearly visible as when the SOG graph flats out at close to zero value. These periods are highlighted with green background color.

As the ship cruised between stops, the heading direction was about 190° . During the measurements, the heading direction was 240° at stop 2.1, roughly 140° at stop 2.2-2.5 and about 315° at stop 2.6. The wind direction was almost constantly 45° over the six-hour period. It is clear that the ship was oriented approximately perpendicular to the wind direction when it drifted freely during the stops, except from stop 2.1 where the high ice concentration most likely prevented the ship from rotating. For stop 2.2-2.5, the wind came in on port side of the vessel, while it came in from starboard side at stop 2.6.

There is generally a good agreement between forecasted and measured wind direction (WD) and

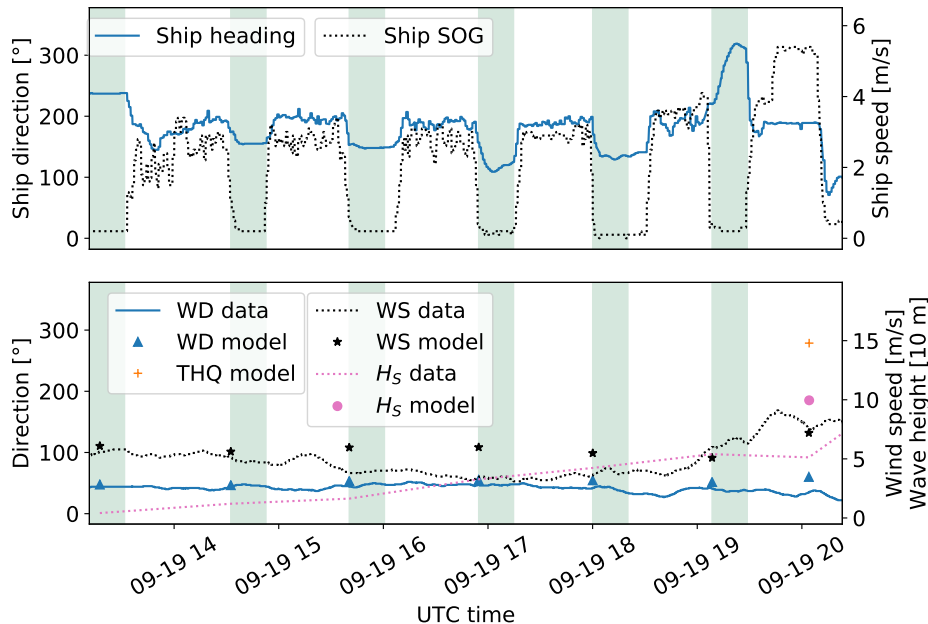


Figure 8: Comparison of observations and WAM-4 model. Ship heading and SOG (upper), and wind direction (WD) and wind speed (WS) from ship measurements and model, total mean wave direction THQ from model and significant wave height H_S (multiplied with a factor of 10) from bow measurements and model (lower). Directions increase clockwise from geographic north (zero degrees). Times with valid data are shaded.

speed (WS), although the model overestimated WS by 50-75% in the period from roughly 15:30 to 18:30. THQ from model and H_S from model and bow measurements are also presented in the lower panel of Fig. 8. The overestimated wind speed could possibly explain why forecasted H_S is 95% higher than measured value at 20:09 when wave model data were available, as WAM-4 is forced with winds at 10m height from the atmospheric model UM4. Also, occasional ice floes were observed at this point and WAM-4 does not take attenuation caused by the presence of ice into considerations. However, the measured wave data were saturated at this point and cannot be completely trusted. THQ was 282.1° at 20:09. Due to the low variation in THQ (in time and space) over the period when attenuation measurements were sampled, as seen in Fig. 7, this value (282.1°) is used to find the WTD through the MIZ, presented in Table 1 and Fig. 1b. The wave heading angle β was 40° at stop 2.1, 140° at the four intermediate stops 2.2-2.5 and 35° at stop 2.6. Wave heading angle will be further assessed in Section 4.

Power spectra from bow measurements (black) and WII instruments (blue) with their respective 95% confidence intervals are compared in Fig. 9, going successively from stop number 1.1 (upper panel) to 1.4 (lower panel). The power spectra from the two methods are consistent for most frequencies in the two first samples closer to the open ocean. The third sample is consistent for some frequencies up to 0.09 Hz. For higher frequencies, the WII spectrum flattens out while the bow spectrum peaks at 0.1 Hz. Investigation of bow spectra from samples taken respectively twenty and forty minutes after the PSD presented here while the ship was still stationary around the WII instruments, reveals similar spectral peaks at the same frequency. This consistency substantiates the validity of the bow measurements. A discussion on this discrepancy follows in Section 4. The fourth sample furthest into the ice displays a fair agreement between the two methods.

Integrated parameters from the spectra in Fig. 9 are summarized in Table 3. There is a good match for both significant wave height and mean period where MPEs do not exceed $\pm 10\%$ for all stops except 1.3 where the error in H_S is -87.8% . We use MPE as defined in (11), although it is not strictly a mean error in this context where only single point parameters are compared.

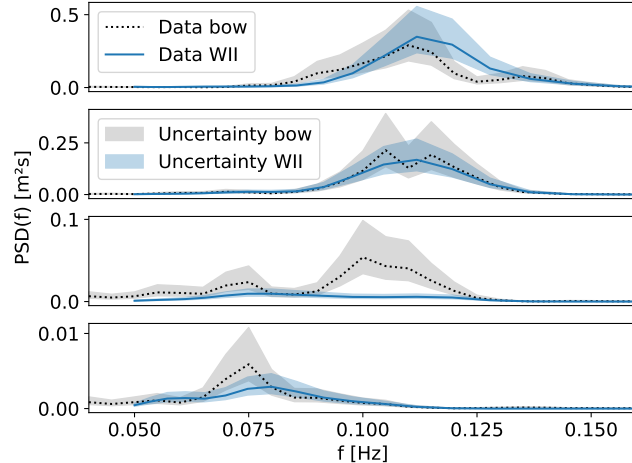


Figure 9: Validation of bow measurements in the MIZ with WII instruments placed on ice floes. PSD are presented from bow measurements (black) and from WII instruments (blue) with their respective 95% confidence intervals as shaded regions, going further into the ice zone from upper (stop 1.1) to lower panel (stop 1.4).

Stop	Significant wave height			Mean wave period		
	H_{S_bow} [m]	H_{S_WII} [m]	MPE [%]	T_{m02_bow} [s]	T_{m02_WII} [s]	MPE [%]
1.1	0.36	0.39	8.4	8.85	8.65	-2.4
1.2	0.29	0.28	-4.3	9.03	9.12	1.0
1.3	0.16	0.09	-87.8	10.14	10.89	6.9
1.4	0.04	0.04	-5.1	11.36	12.57	9.6

Table 3: Significant wave height and zero up-crossing period from bow measurements inside the MIZ are compared with WII measurements. Errors are included.

3.2 Wave attenuation

One dimensional power spectra of the surface elevation with 95% confidence intervals from stops 2.1-2.6 are presented in Fig. 10. Most of the energy is found at either low (swell) or high (wind wave) frequencies. Averaged peak frequency is found to be 0.076 Hz for swell and 0.128 Hz for wind wave. Spectral amplitudes $a(f_0)$ for a set of six finite frequency bins are found from (8) and investigated at stops 2.1-2.6. The highest and lowest f_0 are set to 0.076 Hz and 0.128 Hz respectively. Four intermediate forcing frequencies are evenly distributed between the swell and wind wave frequency.

It is evident that wave energy content increases as the ship approaches the open ocean. Figure 11a shows an exponential decrease in H_S (with 95% confidence intervals) as function of WTD through the MIZ for stops 2.1-2.6. Ideally, the measurements should have been performed simultaneously to ensure stationary wind forcing throughout the attenuation run. Fortunately, wind conditions did not change dramatically over the period from 13:11 to 19:08 as can be seen in Fig. 8, and we therefore assume the wave generation to be approximately stationary.

Spectral amplitude for swell, the third intermediate wave, and wind wave are plotted versus wave travel distance through the MIZ and presented in Fig. 11b along with their 95% confidence intervals. A clear exponential attenuation for wind wave can be seen. The exponential shape is less obvious for the intermediate frequency and swell, but the trend is visible. Also, swell amplitude seems to decrease from stop 2.5 to 2.6, which is not physical, and this problem is addressed in Section 4. Exponential fits lie within the confidence intervals of $a(f_0)$ for almost all frequencies.

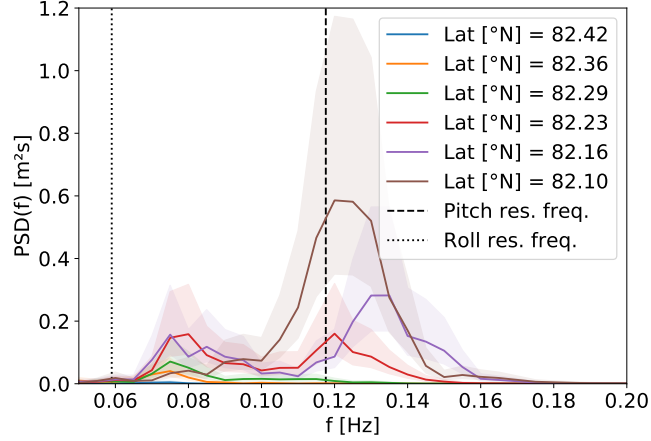
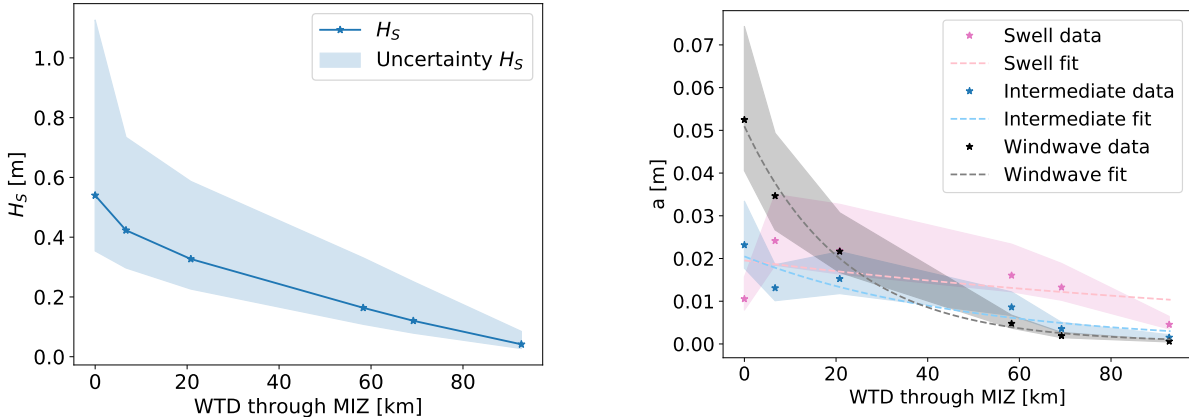


Figure 10: Power spectra at different latitudes with 95% confidence intervals, and ship resonance frequencies in vertical modes from Ytterland (2016).



(a) H_S versus wave traveling distance into the MIZ. (b) $a(f_0)$ versus wave traveling distance into the MIZ.

Figure 11: Wave damping with 95% confidence intervals. a) Significant wave height H_S . b) Spectral amplitudes $a(f_0)$ for swell, one of the intermediate wave frequencies and wind wave. Exponential decay functions are fitted to the data.

The spatial damping coefficients α are plotted versus their respective f_0 with black asterisks in Fig. 12. Squire & Moore (1980) investigated attenuation in the Antarctic and went approximately the same distance into the MIZ as in the present study. In Squire & Moore (1980), α was found to be $2.72 \times 10^{-5} \text{m}^{-1}$ and $4.38 \times 10^{-5} \text{m}^{-1}$ for the central periods 12.2 s and 9.4 s respectively. We obtain $0.88 \times 10^{-5} \text{m}^{-1}$ and $2.15 \times 10^{-5} \text{m}^{-1}$ i.e. 51-67% lower values when interpolating to the same periods. Wave attenuations increase with higher frequencies, from $0.68 \times 10^{-5} \text{m}^{-1}$ at 0.076 Hz to $4.28 \times 10^{-5} \text{m}^{-1}$ at 0.128 Hz, and have the shape of a power function. The fitted power curve is plotted with a dashed gray line and the 1σ uncertainty associated with the power coefficient is marked with a gray shaded area in Fig. 12. The standard error in the fitted exponent is 3.39 ± 0.36 .

Values of α obtained from (13) are plotted with a blue line in Fig. 12. The two-layer model of Sutherland *et al.* (2019) describes the growth rate of α as function of f quite well for the lower frequencies up to about 0.09 Hz, while it slightly overestimates the growth rate for frequencies above 0.10 Hz.

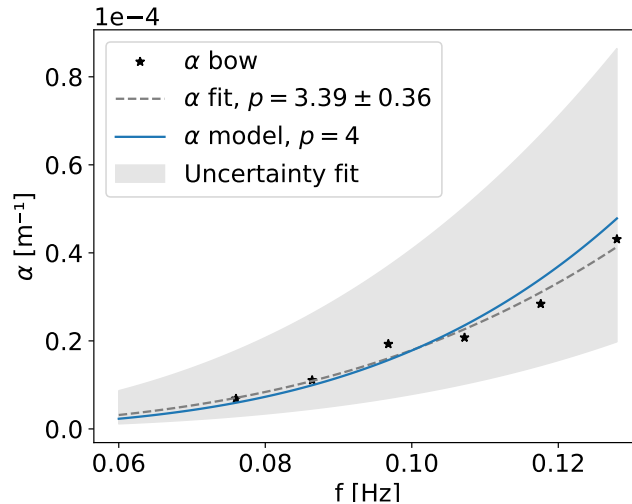


Figure 12: Spatial damping coefficient α as function of frequency from measurements (black) and two-layer model (blue). Power coefficients for the fitted curve and the model are displayed in the legend. 1σ errors associated with the power coefficient estimate for the fitted curve (gray) are shown as the gray shaded region.

4 Discussion

A culture of sharing the design of instruments within the scientific community would enable a more cost effective and increased quantity of data collection in the Arctic. We would like to stimulate researchers to use off-the-shelf sensors and open-source code and therefore make all our material available (See Appendix A). The components used to obtain wave data in this study are relatively cheap compared to industry made black-box instruments. The system can record autonomously, hence, expensive expedition time does not have to be allocated as measurements can be done in parallel. Other devices such as floaters and buoys offer the advantage of multiple simultaneous measurements at different locations, which is not possible with bow mounted sensors. However, bow mounted sensors do not require costly and time-consuming deployment and retrieval operations, and there is low risk associated with losing instruments at sea.

Data recorded while a ship is in motion will contain a Doppler shifted frequency according to the wave heading angle β (Collins III *et al.*, 2017), which could be problematic in the calculation of periods. Peak and mean periods were reported strongly biased by the Doppler shift in Christensen *et al.* (2013), while the estimates of significant wave heights were reasonable since they only depend on the sea surface variance. In the present study, we consider the measurements invalid either when the ship is cruising (and a Doppler shift could be introduced depending on β) or when the UG is saturated (exceeded measure range), as we have not differentiated between these two cases. We see little difference in MAPE inside versus outside the time periods we consider valid, when comparing periods from bow measurements with WAM-4. MPEs are actually higher in the periods where data is considered valid. There is also a slightly better match outside the valid periods in the comparison of significant wave height. This is somewhat counter intuitive, but there is of course uncertainty associated with the spectral model, and β is not included in the analysis. It is possible to correct the Doppler shift, but this requires accurate observations of the wave direction, or more precisely β (Collins III *et al.*, 2017). This would allow for possibly improved mean period estimates during cruising. For future expeditions we would recommend to pre-calibrate the UG to allow for a larger sensing window to avoid saturation.

Significant wave energy for $f > 0.1$ Hz was detected by the bow mounted sensors and not by the WII instruments at stop 1.3 as seen in Figure 9. Yiew *et al.* (2016) have performed experiments with thin floating disks and applied two theoretical models to determine the hydrodynamic responses of ice floes with diameter d in regular waves with wavelength λ . They find RAO in heave to be 0.5 at approximately $\lambda/d = 1.5$ and rapidly degreasing for larger λ/d . For the peak frequency measured by

the bow sensor, i.e. $f = 0.1$ Hz, λ is found to be 156 m with Eq. 1. We have no exact measure of the size of the ice floe at stop 1.3, but deeming from Fig. 1a and Fig. 9 in Rabault *et al.* (2019) its diameter seems to be at least in the order of hundred meters. The flexural rigidity of the ice floe will of course differ from the disks applied in Yiew *et al.* (2016), but the results in this paper suggest a low heave response of such a large floe at this short wavelength. As the WII instruments essentially calculate the power spectra from the heave motion of the floe, a plausible explanation for the discrepancy between the two instruments could be that waves in this frequency range were effectively damped by the floe. The bow sensor on the other hand, measured at points where the ice was broken up by the ship and was therefore able to detect higher frequencies and give a more accurate observation of the sea state.

Another relevant problem is the response of the ship itself. Figure 10 shows the resonance frequencies of the ship in the vertical modes with $\beta = 150^\circ/30^\circ$ (due to symmetry) (Ytterland, 2016), which almost corresponds to β at stops 2.1-2.5 (10° deviation) and stop 2.6 (5° deviation). The RAO values are 1.8 and 1.9 for these angles, meaning a possible maximum amplification of 80% and 90% for roll and pitch motion respectively. Heave mode has only got a peak in RAO for $\beta = 90^\circ$, which did not occur during stops 2.1-2.6 and is therefore not shown. None of the spectral peaks in Fig. 10 coincides with the natural frequencies in roll. However, the high frequency peaks are in the same range as the ship's natural frequency in pitch. Pitch motion was likely amplified up to 90% when exposed to 0.12 Hz waves. However, this effect should be compensated for by the pitch motion correction performed on the data.

Stop 2.6 has been included in our wave attenuation analysis even though it was located outside of the defined ice edge in Figure 1b. This ice edge was estimated from coarsely resolved satellite images and is therefore not very accurate. Reflected wave energy from the ice edge could have been a problem at stop 2.6. However, the ice edge was not a strictly defined line, it was rather observed as a gradually decreasing ice concentration towards the open ocean and ice floes were still present around stop 2.6. Swell energy was observed to decrease from stop 2.5 to 2.6 where the opposite is expected. Our assumption of stationary wave field may not have been valid in this case, although wind measurements and WAM-4 model data suggest otherwise. There is also uncertainty associated with the total mean wave direction THQ . There could have been discrepancies between THQ and mean swell direction THQ_{swell} , although $90^\circ < THQ_{swell} < 270^\circ$ (swell travelling south) is unlikely. Another possible explanation is that ship yaw (i.e. rotation in the horizontal plane) and/or a changing β might have influenced the low frequencies in the measurements. At stop 2.6 the ship heading increased continuously from approximately 200° until it stabilized at 315° towards the end of the 20 min sampling period, whereas both ship heading and β were almost constant for the other stops, as seen in Figure 8.

A general issue with wave attenuation models is that model parameters, for example the effective viscosity in the one-layer models of Weber (1987) and Newyear & Martin (1997), are not known a priori but usually obtained from a fit to experimental data. That is also the case in the model of Sutherland *et al.* (2019) where uncertainty is associated with the fractional ice thickness $0 < \epsilon < 1$, which is linked with the sea ice micro-structure. Mechanical properties of ice are particularly difficult to estimate in the MIZ with its heterogenous composition of ice types. However, physical insight of the problem can be found based on our observations. The rather small ϵ value implies that wave motion exists on the order of cm in the ice, which is not ridiculously low considering the large ice thickness. A small ϵ value can be expected for areas with large ice floes as wave motion is negligible where the conditions approach solid ice. Such conditions were encountered deeming from Fig. 1a and from Fig. 9 in Rabault *et al.* (2019). Sutherland *et al.* (2019) also argues that a higher ice concentration will lead to (relatively) cold sea ice which is more impermeable, hence one could expect a small ϵ value.

We emphasize that we are not trying to show a universal power law in Fig. 12, which would not make sense for frequencies spanning over less than a decade, we simply compare the coefficients with the model. The power coefficient fit gives a frequency dependence of $\alpha \propto f^{3.39}$, which is similar to (13) where $\alpha \propto f^4$. Wind energy input is not considered by the model. With a wind speed of approximately 6 m/s on average over the measurement period as seen in Fig. 8, it is reasonable to assume that wave generation has taken place, which will reduce the slope of the observed attenuation at higher frequencies. This could explain why the model predicts the observation quite well for the lower frequency bins, while it overestimates attenuation for the higher frequency bins, based on the six data points.

5 Conclusions

We have presented shipborne wave measurements from the MIZ with a system combining an altimeter (UG) and a motion correction device (IMU). The UG was able to reflect signals off an ice-covered surface. This methodology is both cost effective as components are off-the-shelf and it can be installed on a cruise with other objectives. The system has proven to be robust as instruments have measured continuously over the two-week period without suffering any damage. Our setup provides single point time series of ocean surface elevation outside of and inside the MIZ, which enables us to produce 1D power spectra and integrated parameters.

Measured data have been compared to the WAM-4 spectral wave model over a period of eight days. We have found good agreement in mean and zero up-crossing periods and significant wave height. Mean absolute percentage errors (MAPE) were 18.9%, 15.0% and 17.2% for H_S , Tm_{01} and Tm_{02} respectively during valid measurements (23% of the time). Errors were about the same during periods where measurements were not considered valid, indicating that the system is insensitive to exceeded instrument range and/or Doppler shifted wave frequencies. Forecasted significant wave height was 95% higher than the value measured inside the MIZ. This deviation might have been caused by an overestimated model wind speed compared to wind speed measured with the ship anemometer, or by the fact that occasional ice floes were present, which were not considered by the forecast model. Power spectra and integrated parameters from bow measurements have been compared with values obtained from waves-in-ice instruments placed on ice floes. A good match was found when the sensors were placed on smaller floes further out in the MIZ. The spectra agree fairly well further into the MIZ. A major discrepancy was likely caused by a large ice floe that filtered out higher frequencies where the waves-in-ice instrument was placed. Errors in H_S , Tm_{02} were smaller than 10% in all cases except for one of the measurements.

We observed an exponential wave attenuation when going through the MIZ. The spatial damping coefficients obtained from measurements were comparable (51 – 67% lower) to what was reported in a previous study with a similar wave traveling distance through the ice (Squire & Moore, 1980). We have found a strongly frequency dependent attenuation, where $\alpha \propto f^{3.39}$, which is similar to a two-layer attenuation model where $\alpha \propto f^4$ (Sutherland *et al.*, 2019).

Acknowledgement

The authors are grateful to Øyvind Breivik for inviting us to the cruise. We also thank the crew of RV Kronprins Haakon for their assistance. The Nansen Legacy project helped funding the cruise and loggers. Funding for the experiment was provided by the Research Council of Norway under the PETROMAKS2 scheme (project DOFI, Grant number 28062). The data are available from the corresponding author upon request.

Appendix A: Open source code and designs

All the designs and files used for setting up the system, including the code used to extract and process data, and general instructions for mounting the instruments, are made available on the Github of the author under a MIT license that allows full re-use and further development (https://github.com/jerabaul29/Ultrasound_IMU_boat_waves_system [Note: The material will be available upon publication in peer-reviewed literature]). All software and designs are based entirely on open source tools, so that the designs can be easily modified and built upon.

References

- CARRASCO, ANA & GUSDAL, YVONNE 2014 Validation of the operational wave model wam for the years 2012 and 2013. *Tech. Rep.*. Section of Ocean and Ice, Norwegian Meteorological Institute.
- CHRISTENSEN, KAI HÅKON, RÖHRS, JOHANNES, WARD, BRIAN, FER, ILKER, BROSTRÖM, GÖRAN, SAETRA, ØYVIND & BREIVIK, ØYVIND 2013 Surface wave measurements using a ship-mounted ultrasonic altimeter. *Methods in Oceanography* **6**, 1–15.

- COLLINS III, CO, BLOMQUIST, B, PERSSON, O, LUND, B, ROGERS, WE, THOMSON, J, WANG, D, SMITH, M, DOBLE, M, WADHAMS, P & OTHERS 2017 Doppler correction of wave frequency spectra measured by underway vessels. *Journal of Atmospheric and Oceanic Technology* **34** (2), 429–436.
- EARLE, MARSHALL D 1996 Nondirectional and directional wave data analysis procedures. *NDBC Tech. Doc* **96** (002).
- FELTHAM, DANNY 2015 Arctic sea ice reduction: the evidence, models and impacts.
- FRITZNER, SINDRE, GRAVERSEN, RUNE, CHRISTENSEN, KAI H, ROSTOSKY, PHILIP & WANG, KEGUANG 2019 Impact of assimilating sea ice concentration, sea ice thickness and snow depth in a coupled ocean–sea ice modelling system. *The Cryosphere* **13** (2), 491–509.
- ITTC, SPECIALIST COMMITTEE 2017 Confidence intervals for significant wave height and modal period. *Tech. Rep.*. International Towing Tank Conference, accessed: 2019-08-29.
- MAGNUSSON, ANNE K & DONELAN, MARK A 2013 The andrea wave characteristics of a measured north sea rogue wave. *Journal of Offshore Mechanics and Arctic Engineering* **135** (3).
- MARCHENKO, ALEKSEY, RABAULT, JEAN, SUTHERLAND, GRAIG, COLLINS, CLARENCE O, WADHAMS, PETER & CHUMAKOV, MIKHAIL 2017 Field observations and preliminary investigations of a wave event in solid drift ice in the barents sea. In *Proceedings-International Conference on Port and Ocean Engineering under Arctic Conditions*. Port and Ocean Engineering under Arctic Conditions.
- MEYLAN, MICHAEL H, BENNETTS, LUKE G & KOHOUT, ALISON L 2014 In situ measurements and analysis of ocean waves in the antarctic marginal ice zone. *Geophysical Research Letters* **41** (14), 5046–5051.
- NEWYEAR, KARL & MARTIN, SEELYE 1997 A comparison of theory and laboratory measurements of wave propagation and attenuation in grease ice. *Journal of Geophysical Research: Oceans* **102** (C11), 25091–25099.
- RABAULT, JEAN, SUTHERLAND, GRAIG, GUNDERSEN, OLAV & JENSEN, ATLE 2017 Measurements of wave damping by a grease ice slick in svalbard using off-the-shelf sensors and open-source electronics. *Journal of Glaciology* **63** (238), 372–381.
- RABAULT, JEAN, SUTHERLAND, GRAIG, GUNDERSEN, OLAV & JENSEN, ATLE 2019 An open source, versatile, affordable waves in ice instrument for remote sensing in the polar regions. *arXiv preprint arXiv:1901.02410* .
- RABAULT, JEAN, SUTHERLAND, GRAIG, WARD, BRIAN, CHRISTENSEN, KAI H, HALSNE, TRYGVE & JENSEN, ATLE 2016 Measurements of waves in landfast ice using inertial motion units. *IEEE Transactions on Geoscience and Remote Sensing* **54** (11), 6399–6408.
- REIGSTAD, MARIT, ELDEVIK, TOR & GERLAND, SEBASTIAN 2017 The nansen legacy. scientific exploration and sustainable management beyond the ice edge. overall project plan. <https://arvenetternansen.com/wp-content/uploads/2018/02/Nansen-Legacy-3.0-WEB-2.pdf>, accessed: 2019-08-27.
- REISTAD, MAGNAR, BREIVIK, ØYVIND, HAAKENSTAD, HILDE, AARNES, OLE J, FUREVIK, BIRGITTE R & BIDLOT, JEAN-RAYMOND 2011 A high-resolution hindcast of wind and waves for the north sea, the norwegian sea, and the barents sea. *Journal of Geophysical Research: Oceans* **116** (C5).
- SQUIRE, VERNON A 2007 Of ocean waves and sea-ice revisited. *Cold Regions Science and Technology* **49** (2), 110–133.
- SQUIRE, VERNON A & MOORE, STUART C 1980 Direct measurement of the attenuation of ocean waves by pack ice. *Nature* **283** (5745), 365.
- SUTHERLAND, GRAIG & RABAULT, JEAN 2016 Observations of wave dispersion and attenuation in landfast ice. *Journal of Geophysical Research: Oceans* **121** (3), 1984–1997.
- SUTHERLAND, GRAIG, RABAULT, JEAN, CHRISTENSEN, KAI H & JENSEN, ATLE 2019 A two layer model for wave dissipation in sea ice. *Applied Ocean Research* **88**, 111–118.
- THOMSON, JIM & ROGERS, W ERICK 2014 Swell and sea in the emerging arctic ocean. *Geophysical Research Letters* **41** (9), 3136–3140.
- WADHAMS, PETER, SQUIRE, VERNON A, GOODMAN, DOUGAL J, COWAN, ANDREW M & MOORE, STUART C 1988 The attenuation rates of ocean waves in the marginal ice zone. *Journal of Geophysical Research: Oceans* **93** (C6), 6799–6818.
- WEBER, JAN ERIK 1987 Wave attenuation and wave drift in the marginal ice zone. *Journal of physical oceanography* **17** (12), 2351–2361.
- YIEW, LJ, BENNETTS, LG, MEYLAN, MH, FRENCH, BJ & THOMAS, GA 2016 Hydrodynamic responses of a thin floating disk to regular waves. *Ocean Modelling* **97**, 52–64.
- YOUNG, IR 1995 The determination of confidence limits associated with estimates of the spectral peak frequency. *Ocean engineering* **22** (7), 669–686.
- YTTERLAND, ANDERS 2016 Motion analysis report nvc 395 polar kronprins haakon. *Tech. Rep.*. Ship Design and Systems, Rolls-Royce Marine.